A Hybrid Integration Method for Moving Target Detection With GNSS-Based Passive Radar

Zhenyu He [iD], Yang Yang, and Wu Chen [iD]

Abstract—**Global navigation satellite system (GNSS) based passive radar has been applied in the detection of moving targets. However, the low signal power of GNSS on the earth's surface limits the application of this technology for the long-range or low-observable target detection. Increasing the observation time can effectively improve the detection capability. But the target motion involves the range cell migration (RCM) and the Doppler frequency migration (DFM) over the long observation time, which results in the integration gain loss and lower the detection performance. This article proposes a new hybrid coherent and noncoherent integration method named the keystone transform and Lv's distribution. The proposed method not only compensate the RCM and the DFM but also provide coherent and noncoherent integration gains to increase the signal-to-noise ratio. The simulated results and the field trial results demonstrate that the detection performance of the proposed method is superior to the other two known moving target detection methods. And the analysis of the computational complexity shows that the proposed method and the other two methods are in the same order of $O(N^3 \log N)$.**

Index Terms—**Global navigation satellite system (GNSS) based passive radar, keystone transform (KT), long-time hybrid integration, Lv's distribution.**

I. INTRODUCTION

WITH the development of wireless technology, many radio sources are employed as the noncooperative transmitters for passive radar applications. A passive radar system without a dedicated transmitter has merits of low-cost, license-free, covertness, and no electromagnetic pollution because only the receiving segment is needed. Passive radar systems become promising alternatives to the traditional active ones that need heavy transmission devices. Several contributions are found in the recent studies based on the different kinds of terrestrial illuminators, such as digital video broadcasting terrestrial [1], frequency modulated radio [2], GSM [3], and WiMAX base stations [4]. The terrestrial-based sources allow the long-range detection due to the adequate signal power. However, their applications are

The authors are with the Department of Land Surveying and Geo-Informatics, Hong Kong Polytechnic University 999077, Hong Kong, and also with Shenzhen Research Institute, The Hong Kong Polytechnic University, Shenzhen 518057, China (e-mail: zhenyu.he@connect.polyu.hk; yyang.yang@connect.polyu.hk; wu.chen@polyu.edu.hk).

limited in coastal areas or open seas because the broadcasting antennas face the users on land. Compared with the terrestrial-based transmitters, satellites can provide the global and persistent coverage, such as digital video broadcasting-satellite, and global navigation satellite systems (GNSS). GNSS is one of the most popular satellite-based passive radar systems, including global positioning system (GPS), global navigation satellite system (GLONASS), Galileo system, and Beidou system. This article concentrates on the GNSS-based passive radar system.

Many studies on the GNSS-based passive radar were made over the last years. Most of them focused on the static objects on land or monitoring temporal scene changes [5]–[13]. However, a few studies deal with moving objects. Recent proof-of-concept experiments of GNSS-based passive radar for the maritime moving target detection (MTD) were conducted [14], [15], which demonstrated the feasibility of the concept. The main drawback of the GNSS-based passive radar is that the signal power density on the earth's surface is as low as -135 dBW/m^2 [16]. Therefore, the reflected target signals are usually contaminated by the background noise. To overcome such problem, long integration time is an effective way to increase the target signal power [17]. However, the target motion cannot be ignored over the long observation time, which results in the target signal migration through the resolution cells, such as the range cell migration (RCM) and the Doppler frequency migration (DFM). The occurring migration will reduce the integration performance. To increase the coherent processing interval (CPI) in the case of the target motion, some coherent integration methods have been proposed, such as the Radon Fourier transform [18] and the Radon fractional Fourier transform (FrFT) [19]. However, they consider an active radar system where the CPI in an order of few seconds is sufficient for the low-observable target detection. While, in the GNSS-based passive radar, obtaining a suitable signal-to-noise ratio (SNR) of the target signal requires up to several tens of seconds. The full coherent integration methods are not feasible during the long observation time because the target scattering mechanism cannot be regarded as coherent [20]. Noncoherent integration methods do not require the strict coherence and are easy to be achieved. The Hough transform-based methods [21]–[23] are typical. But the noncoherent integration methods do not compensate the phase fluctuation of the target signal, which fails to be applied in the weak target signal detection due to the integration gain loss. Therefore, the MTD techniques based on the active radar systems are not suitable for the GNSS-based passive radar.

In the recent years, some proposed the strategy of hybrid coherent and noncoherent integration technique applied in the

GNSS-based passive radar [20], [24], [25]. The collected data in the long observation time are first divided into multiple frames. Each frame has a relatively short CPI so that the fluctuations in the target's radar cross section (RCS) are negligible. Then, the coherent integration methods are used for each frame. Finally, multiple frames are noncoherently combined for further SNR improvement. The difference is that they adopt different methods for the RCM and the DFM compensation as well as the coherent integration. In [24], the fast Fourier transform (FFT) is used as the coherent integration method, which corresponds to the classic MTD technique. Then, a target motion compensation (TMC) searching for the chirp rate is employed to compensate the RCM and the DFM between the frames. This method was further developed in [25] by taking the DFM inside the frame into account because of the high Doppler frequency resolution. The proposed method in [24] and [25] can be regarded as the polynomial Fourier transform (PFT) [26], [27] since the chirp rate needs to be searched. While Li *et al.* [20] exploit the keystone transform (KT) to remove the RCM. Then, the FrFT searching for the rotation angles allows the coherent integration in the centroid frequency and chirp rate (CFCR) domain for each frame and corrects the DFM inside the frame. Finally, the chirp rate candidates in the CFCR domain are used for the DFM alignment between the frames before the noncoherent integration operation.

Motivated by the previous work, this article adopts the strategy of hybrid integration and proposes a new target detection method known as the Keystone transform and Lv's distribution (KT+LVD). The KT can remove the RCM without knowing the target's velocity in advance. And the LVD provides the coherent integration gain for each frame in the CFCR domain and compensates DFM inside the frame simultaneously without searching. Compared with the PFT and the FrFT, the LVD can provide higher signal concentration ratio and lower sidelobes [28], [29], which is desired for the target detection in the large background noise. Then, a Doppler frequency alignment operation is employed to eliminate DFM between multiple frames. Finally, noncoherent integration is performed for further target signal power concentration. The computational complexity of the proposed method is analyzed and compared with the other two known target detection methods in [20], [24], and [25]. The comparison results show that the computational burden of the proposed method is in the same order as the above two methods. Numerical experiments in a simulation and field trials are carried out to validate the proposed method. The results of both the simulation and the field trials demonstrate that the proposed method is superior to the above two methods in terms of the detection capability.

The article is organized as follows. Section II introduces the bistatic geometry and the signal model. Section III describes the processing procedure of the proposed method and analyzes the computational complexity. Section IV reports the simulated results and the field trial results. Finally, some conclusions are given in Section V.

II. BISTATIC GEOMETRY AND SIGNAL MODEL

Fig. 1 shows the bistatic acquisition geometry of this passive radar system. The receiver (R_x) on the shore has a
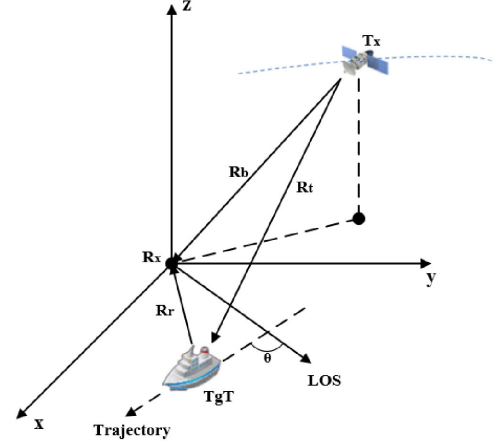

Fig. 1. Bistatic acquisition geometry for GNSS-based passive radar in maritime surveillance.

pair of channels: the reference channel (RC) collects the direct signal from the satellite (T_x) as a reference signal, while the surveillance channel (SC) records the reflected signals from the moving target (TgT) on the sea. The instantaneous ranges between T_x, R_x, and TgT are as follows: R_t is the T_x-TgT range, R_r is the TgT-R_x range, and R_b is the baseline length between T_x and R_x. Because range compression in the passive radar system is obtained by matched filtering with the reference signal compensating the instantaneous delay between T_x and R_x, the bistatic range history of the moving target is defined as

$$R_{bi}\ (t_m) = R_t\ (t_m) + R_r\ (t_m) - R_b\ (t_m).\qquad(1)$$

In this article, we assume a maritime target moving at almost constant velocity. This assumption is reasonable for the ships sailing at cruising speed [25]. Hence, the phase term of the received target signal can be approximated as quadratic during the observation time [20], [24], [25]. While maneuvering target has higher phase term and is beyond the scope of this article, the bistatic range history can be rewritten as

$$R_{bi}\ (t_m) = \lambda \left(\frac{\gamma}{2} \times t_m^2 + f_0 \times t_m + \frac{R_0}{\lambda} \right)\qquad(2)$$

where λ is the carrier wavelength, γ is the Doppler chirp rate, f_0 is the Doppler centroid, and $R_0 = R_t\ (0) + R_r\ (0) - R_b(0)$ is the initial bistatic range.

The direct signal in the RC is usually very noisy, the SNR of which can be as low as -40 dB [10]. Signal synchronization can generate the noise-free replica of the direct signal as the local reference signal [5]. Here, taking GPS L1 signal for example and ignoring constant phase and amplitude terms, we can express the local reference signal as radar data formatting

$$S_d\ (t, t_m) = C\ (t - \tau_d) \times D\ (t - \tau_d) \times e^{j(2\pi f_d t + \varphi_d(t_m))}\qquad(3)$$

where $t \in [0,\ \text{PRI}]$ is the fast-time, PRI is the pulse repetition interval (i.e., the duration time of C/A code), $t_m \in [-\frac{T}{2}, \frac{T}{2}]$ is the slow-time, T is the entire observation time, $C(\cdot)$ is C/A code, $D(\cdot)$ is the navigation data, and $e(\cdot)$ is the complex carrier. τ_d, f_d and $\varphi_d(t_m)$ are the code phase delay, carrier Doppler frequency and carrier phase term of the local reference signal, respectively. Their values are dependent on the relative position
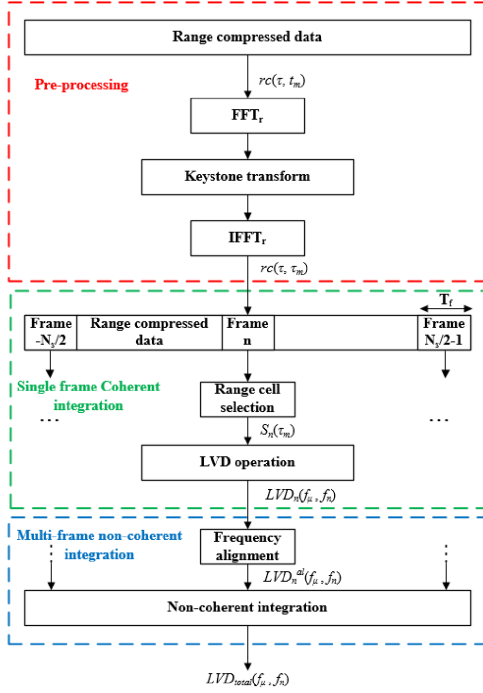
Fig. 2.   Processing flowchart of the MTD technique.

and the movement between Tx and Rx. Moreover, τ_d and $\varphi_d(t_m)$ contain the total delay and phase errors, respectively, induced by the atmospheric factors (i.e., troposphere and ionosphere delay) and the receiver errors (i.e., clock cycle slips and local oscillator drift). Likewise, assuming one target case, we can express the target signal in the SC as

$$S_r\ (t, t_m) =\ C\ (t - \tau_r) \times D\ (t - \tau_r) \times e^{j(2\pi f_r t + \varphi_r(t_m))} \tag{4}$$

where τ_r, f_r, and $\varphi_r(t_m)$ are the code phase delay, carrier frequency, and carrier phase term of the target signal, respectively.

III. MTD TECHNIQUE

Due to the low GNSS signal power on the earth's surface, target signals are usually very weak and affected by the background disturbance. Increasing the observation time is an effective way to improve the target detection probability. However, on one hand, the target motion gives rise to the RCM and DFM during the long observation time. On the other hand, the fluctuations of the target's RCS cannot be ignored. To overcome these issues, the strategy of hybrid coherent and noncoherent integration is employed in [20], [24], and [25]. Hence, this article also adopts this strategy. The processing flowchart of the proposed method is presented in Fig. 2, which includes three main stages. Each stage is described in the following. Moreover, the computational complexity of the proposed method is analyzed and compared with the other two MTD methods proposed in [20], [24], and [25]. For convenience, the method proposed in [24] and [25] is called MTD and target motion correction (MTD+TMC), while the method proposed in [20] is called keystone transform and fractional Fourier transform (KT+FrFT).

A. Preprocessing

Range compression is conducted with the cross-correlation function between the local reference signal in (3) and the target signal in (4), thus obtaining

$$rc\ (\tau, t_m) = \int S_d^*\ (t - \tau, t_m) \times S_r\ (t, t_m)\, dt$$

$$= \int C\ (t - \tau_d - \tau) \times C\ (t - \tau_r)$$

$$\times D\ (t - \tau_d) \times D\ (t - \tau_r)$$

$$\times e^{j(2\pi \Delta f(t_m)t + \Delta\varphi(t_m))} dt \tag{5}$$

where $*$ is the complex conjugate, $\Delta f(t_m)$ and $\Delta\varphi(t_m)$ are the instantaneous difference between the local reference signal and the target signal with respect to carrier Doppler frequency and phase, respectively. Note that: 1) $D(t - \tau_d) \times D(t - \tau_r)$ equals 1 within the range of 6000 km [7]; 2) $\Delta f(t_m)$ can be neglected due to the low Doppler frequencies induced by the moving target during the PRI [25]; 3) $\Delta\varphi(t_m)$ eliminates the total phase errors, induced by the atmospheric factors and the receiver errors due to the similar atmospheric factors and the shared oscillator in the RC and SC [25]. Therefore, after integral operation, (5) can be derived as

$$rc\ (\tau, t_m) =\ CF\left(\tau - \frac{R_{bi}(t_m)}{c}\right) \times e^{-j2\pi \frac{f_c}{c} R_{bi}(t_m)} \tag{6}$$

where $CF(\cdot)$ denotes the envelope of the cross-correlation function, $R_{bi}(t_m)$ is the bistatic range defined in (1), f_c is the central carrier frequency, and c is the speed of light. From (6), we can find that the varying bistatic range in the cross-correlation function and the exponential phase term results in the RCM and DFM, respectively. For the long observation time, both the RCM and the DFM should be tackled and corrected before coherent and noncoherent integration.

Since the KT can compensate the range migration without knowing the target velocity in advance [30], the RCM is first corrected. To apply the KT in the RCM correction, the range-compressed target signal in (6) goes in the range-frequency and slow-time domain by Fourier transform (FT), which is derived as

$$rc\ (f_r, t_m)\ =\ CF(f_r) \times e^{-j2\pi \frac{f_r + f_c}{c} R_{bi}(t_m)} \tag{7}$$

where f_r is the range-frequency component. By inserting (2) into (7), we have the exponential phase term of (7) as

$$\Phi_{rc}(f_r, t_m) =\ -2\pi\left(\frac{\gamma}{2} \times \frac{f_r + f_c}{f_c} \times t_m^2 + \frac{f_r + f_c}{f_c} \times f_0 \times t_m\right.$$

$$\left. + \frac{f_r + f_c}{c} \times R_0\right). \tag{8}$$

Equation (8) shows that the range-frequency and the slow-time have the coupling with each other, which results in the RCM. To remove the coupling, the KT performs a scaling operation in the (f_r, t_m) domain

$$f_c \times \tau_m = (f_r + f_c) \times t_m \tag{9}$$

where τ_m is the rescaled slow-time. Substituting (9) into (8), we have the rescaled phase term as

$$\Phi_{rc}(f_r, \tau_m) = -2\pi \left(\frac{\gamma}{2} \times \frac{f_c}{f_r + f_c} \times \tau_m^2 + f_0 \times \tau_m \right.$$
$$\left. + \frac{f_r + f_c}{c} \times R_0 \right). \tag{10}$$

Since the GNSS signal is not designed for the radar purpose, the narrow band of GNSS ranging code makes $f_r \ll f_c$. We have $f_c/(f_r + f_c) \approx 1$, and (10) can be rewritten as

$$\Phi_{rc}(f_r, \tau_m) = -2\pi \left(\frac{\gamma}{2} \times \tau_m^2 + f_0 \times \tau_m + \frac{R_0}{\lambda} \right)$$
$$- 2\pi \left(\frac{f_r}{c} \times R_0 \right). \tag{11}$$

As shown in (11), the first brackets correspond to the quadratic phase term of the target signal along the slow-time domain, while the second brackets show that the RCM is compensated into the constant bistatic range. After range inverse FT for (7), the range-compressed target signal in (6) is rewritten as

$$rc(r, \tau_m) = CF \left(r - \frac{R_0}{c} \right) \times e^{-j2\pi \left(\frac{\gamma}{2} \times \tau_m^2 + f_0 \times \tau_m + \frac{R_0}{\lambda} \right)}$$
$$\tag{12}$$

where $r = \tau \times c$ is the range cell. The above procedure allows the coupling effects of the linear RCM removed. But the residual nonlinear RCM is still present. The effect of nonlinear RCM is expected to be smaller than one range resolution cell due to the coarse range resolution of this passive radar system. Now, the range-compressed target signal power is located at one range cell so that the following coherent integration can be implemented along the slow-time domain. Fig. 3 shows an example for the noise-free range compression result before and after the RCM correction by the KT. Compared with the severe RCM in Fig. 3(a), Fig. 3(b) shows that the envelopes along the slow-time samples are located at the same range cell.

B. Coherent Integration for Single Frame by the LVD

After the preprocessing, the range compression result in (12) is divided into N_s frames along the slow-time dimension. Each frame has the same CPI in an order of seconds so that the RCS fluctuations are negligible. We assume that the target signal is located at the rth range cell. The target signal during one CPI is derived as

$$S_n(\tau_m) = \sigma_n \times rect \left(\frac{\tau_m - n \cdot T_s}{T_s} \right)$$
$$\times e^{-j2\pi \left(\frac{\gamma}{2} \times \tau_m^2 + f_0 \times \tau_m + \frac{R_0}{\lambda} \right)} \tag{13}$$

where $n \in [-N_s/2, N_s/2 - 1]$, $T_s = T/N_s$ is the length of CPI, σ_n denotes the cross-correlation function's envelope, and $rect(\cdot)$ denotes the time window of the target signal. The exponential phase term in (13) is quadratic, which means the target signal is a linear frequency modulation (LFM) signal along the slow-time dimension.
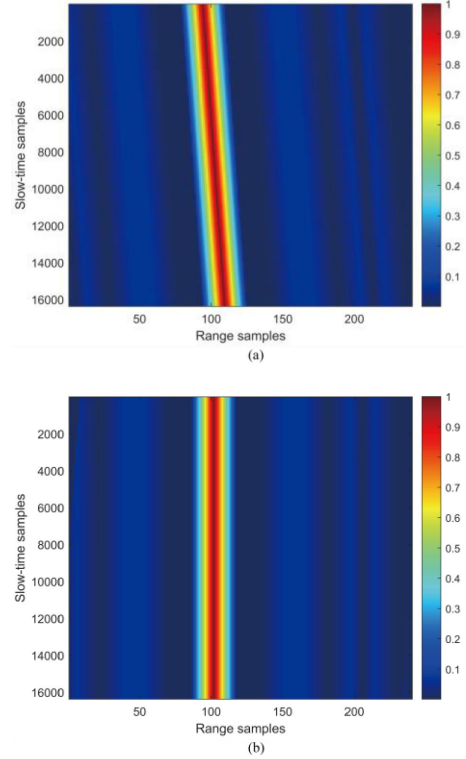

Fig. 3. (a) Noise-free range compression before RCM correction. (b) Noise-free range compression after RCM correction.

The LVD can provide excellent signal concentration for the LFM signal in the CFCR domain [28], [29]. In this section, the LVD is applied to perform coherent integration and compensate DFM occurring inside the single frame. The implementation of the LVD is simple as shown in Fig. 5, including three main steps: parametric symmetric instantaneous autocorrelation function (PSIAF), scaling operation, and two-dimensional FT (2-D FT). The detailed derivation is shown in the following. The PSIAF of (13) is defined as

$$R_n^c(\mu, \tau_m) = S_n \left(\tau_m + \frac{\mu + a}{2} \right) \times S_n^* \left(\tau_m - \frac{\mu + a}{2} \right)$$
$$= \sigma_n^2 \times e^{-j2\pi f_0(\mu+a)} \times e^{-j2\pi\gamma(\mu+a)t_m} \tag{14}$$

where μ is the lag variable and a is a constant time-delay. Equation (14) shows that the slow time τ_m and lag variable μ couple with each other in the second exponential phase term, which is similar to the coupling in (8). To remove the coupling, a scaling operator Γ of a phase function G is defined as

$$\Gamma[G(\mu, \tau_m)] \rightarrow G \left(\mu, \frac{\tau_n}{h(\mu + a)} \right) \tag{15}$$

where τ_n is called the scaled time and h is a scaling factor. According to [28] and [29], we select the parameters $a = 1$ and $h = 1$ to achieve a desirable representation. Applying the scaling operation Γ to (14), we have

$$\Gamma[R_n^c(\mu, \tau_n)] = \sigma_n^2 \times e^{-j2\pi f_0(\mu+1)} \times e^{-j2\pi\gamma\tau_n}. \tag{16}$$
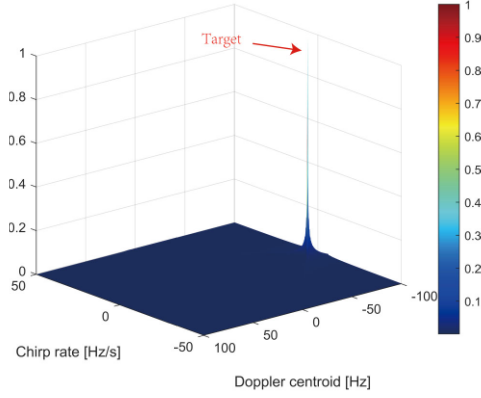
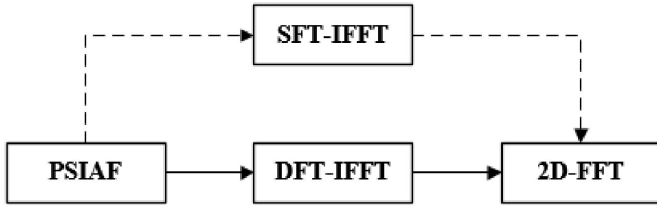Fig. 4.   Coherent integration by the LVD.

Fig. 5.   Implementation of the LVD by two methods.

Then, we perform 2-D FT on (16) in terms of μ and τ_n and obtain the LVD as

$$LVD_n\ (f_\mu,\ f_n) = \sigma_n^2 \times \delta\,(f_\mu - f_0) \times \delta\,(f_n - \gamma) \times e^{-j2\pi f_0} \tag{17}$$

where δ is the impulse function. The coherent integration effect of the LVD is presented in Fig. 4. We can observe that the target signal power has been coherently integrated as a peak in the CFCR domain. The peak values correspond to the chirp rate and the Doppler centroid of the target signal during the CPI, which imply that DFM inside the single frame has been compensated.

The coherent integration gain achieved by the LVD is adequate for high-RCS target detection, whereas low-RCS targets cannot be extracted from the background disturbance by this integration gain. To overcome this problem, the next stage is to conduct a proper noncoherent integration of multiple frames for further SNR improvement enabling target detection.

C. Noncoherent Integration for Multiframe

Because frames start from different observation time, after coherent integration by the LVD, the peaks of the target signals are located at different positions in the CFCR domain. Obviously, a proper Doppler centroid alignment operation should be performed to enable the noncoherent integration for multiframe, which is based on the assumption used in [20], [24], and [25] that the chirp rate of the moving target is a constant during the overall observation time.

Let us select one frame as the reference frame (here assumed to be the $n = 0$ frame). Then, the Doppler centroid of nth frame is aligned to the reference frame by

$$\Delta f_0^n\ (\gamma^*) = \gamma^* \times \text{n} \times T_f \tag{18}$$

where γ^* is the chirp rate varying in the LVD. After Doppler centroid compensation, each frame is expressed as

$$\text{LVD}_n^{al}\ (f_\mu,\ f_n) = \text{LVD}_n\ (f_\mu - \Delta f_0^n\,(\gamma^*),\ f_n). \tag{19}$$

Once the Doppler centroids have been aligned, the peaks of the target signals are located in the same position over the N_s frames. Finally, N_s frames can noncoherently be integrated as

$$\text{LVD}_{\text{total}}\ (f_\mu,\ f_n) = \frac{1}{N_s} \sum_{n\,=\,\frac{-N_s}{2}}^{n\,=\,\frac{N_s}{2}\,-1} \text{LVD}_n\,(f_\mu,\ f_n). \tag{20}$$

After noncoherent integration, the presence of the moving targets can be sought in the integrated map, thanks to the SNR improvement.

D. Computational Complexity Analysis

In this section, we first analyze the computational complexity of the proposed method. Then, the computational complexities of the MTD+TMC and the KT+FrFT are provided to show that the computational burden of the proposed method is the same as the other two. Note that because signal synchronization, range compression, and noncoherent integration are the common steps in all these methods, the computational complexities of these steps are not considered here.

Denote the number of range cells, slow-time samples, lag samples in the proposed method, searching chirp rates in [24] and [25], and searching rotation angles in [20] by N_r, N_t, M', M'', M''', respectively. For the KT, the key implementation step is the scaling operation. The scaling operation can be accomplished by discrete FT and inverse FFT (DFT-IFFT) or chirp-z-transform and IFFT (CZT-IFFT) [31]. Suppose that the calculation of FFT over n needs the computational complexity in the order of $O(N \log N)$ [32], the total complexities of the KT based on the DFT-IFFT and the CZT-IFFT are $O(N_r N_t^2 + 2N_r N_t \log N_r)$ and $O(4N_r N_t \log N_t + 2N_r N_t \log N_r)$, respectively. Similar to the KT, the scaling operation in the LVD can be fulfilled by using the DFT-IFFT or scaled FT and IFFT (SFT-IFFT) [28], [29], corresponding to the order of $O(M N_t^2)$ and $O(4M' N_t \log N_t)$, respectively. Fig. 5 presents two implementation methods for the LVD. Therefore, the overall complexities of the LVD based on the DFT-IFFT and the SFT-IFFT for all range cells are, respectively, $O(M' N_r N_t^2 + M' N_r N_t \log N_t + M' N_r N_t \log M')$ and $O(4M' N_r N_t \log N_t + M' N_r N_t \log N_t + M' N_r N_t \log M')$. Obviously, the latter implementation methods for both the KT and the LVD have lower computational burden than the former, which are more suitable for the modern parallel digital signal processing devices.

In [24] and [25], the required computational complexity of the MTD+TMC is $O(M'' N_r N_t \log N_t + 2M'' N_r N_t \log N_r)$. In [33], the FrFT needs the computational complexity of $O(4M''' N_r N_t \log N_t)$. For a comparison, assume that M', M'', and M''' are in the same order of $O(M)$. The detailed computational complexities of the above three methods are listed
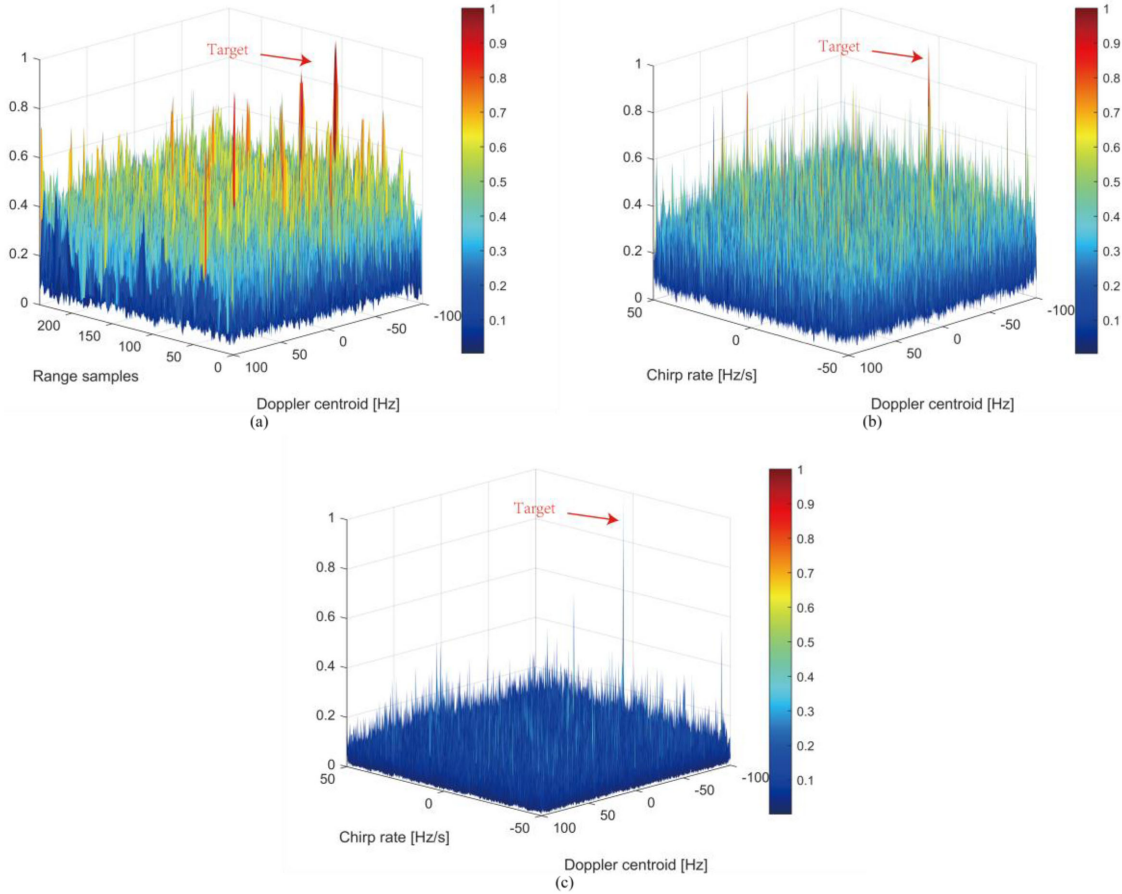
Fig. 6. Hybrid integration for a weak target signal via the MTD+TMC, the KT+FrFT, and the proposed method. (a) MTD+TMC result. (b) KT+FrFT result. (c) Proposed method result.

TABLE I
COMPUTATIONAL COMPLEXITIES OF THE THREE METHODS

Methods	Computational complexity
MTD+TMC	$O(MN_rN_t \log N_t + 2MN_rN_t \log N_r)$
KT+FrFT	$O(4MN_rN_t \log N_t + 2N_rN_t \log N_r$ $+ 4N_rN_t \log N_t)$
The proposed method	$O(4MN_rN_t \log N_t + MN_rN_t \log N_t$ $+ MN_rN_t \log M$ $+ 2N_rN_t \log N_r$ $+ 4N_rN_t \log N_t)$

in Table I. Suppose that $M = N_r = N_t = N$, Table I illustrates that the above three methods are all in the same order of $O(N^3 \log N)$.

IV. SIMULATION AND EXPERIMENTAL RESULTS

In this section, simulation and field trials are conducted to present the effectiveness of the proposed method. Comparisons with the MTD+TMC and the KT+FrFT are also provided to show that the proposed method has a superior detection capability.

A. Simulated Results

The simulation system is assumed as noise-limited rather than clutter-limited, which is well in line with the collected

TABLE II
SIMULATION PARAMETERS OF A WEAK TARGET SIGNAL INTEGRATION

GPS signal Parameters	Power density on the ground	-135 dBW/m^2
	Carrier wavelength	0.1902 m
	C/A code frequency	1.023 MHz
	Pulse repetition frequency (PRF)	1000 Hz
Satellite	Satellite elevation angle	45°
	Satellite azimuth angle	0°
	Satellite-to-receiver range	20286000 m
Background noise	Boltzmann constant	1.38×10^{-23}
	Temperature	300 K
	Receiver noise bandwidth	1.023 MHz
	Receiver Noise figure	3.075 dB
Target	Radial velocity of target	10 m/s
	Initial target-to-receiver range	1000 m
	SNR of target signal	-64.76dB
Hybrid integration	Dwell time	16384 ms
	CPI	4096 ms
	Noncoherent integration times	4

experimental datasets in the field trials. Therefore, Gaussian white noise as the background disturbance is added to the target signals, while no sea clutter is considered. Table II lists the detailed parameters for the simulation.

The hybrid integration effect for the weak target signal using the MTD+TMC, the KT+FrFT, and the proposed method is shown in Fig. 6. All of them consider the RCM and the DFM
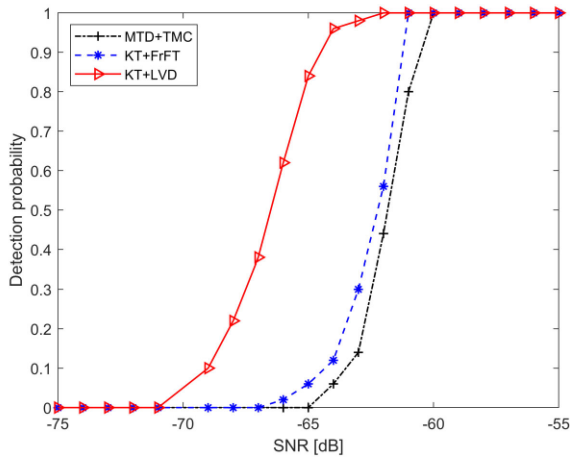
Fig. 7.   Detection probabilities of the three methods.

(a)

(b)

Fig. 8.   (a) Receiver front-end and (b) direct and reflected antennas.

(a)

(b)

Fig. 9.   Photographs of two cargo ships: (a) KUO LIN and (b) WAN HAI 313.

compensation. Compared with Fig. 6(a) and (b), the peak of the target signal in Fig. 6(c) can be easily distinguished from the background noise. The main reason is that the LVD as the coherent integration method provides a high LFM signal concentration ratio, while the FFT and the FrFT used in the other two methods have wide main lobes and high sidelobes, which results in a low signal concentration. Also, we can observe that Fig. 6(c) has a much lower noise level than that in Fig. 6(a) and (b), which implies that the proposed method can achieve a better detection capability than the other two methods.

Monte-Carlo trials are employed to quantitatively evaluate the detection performance of the MTD+TMC, the KT+FrFT, and the proposed method. The constant false alarm rate detector is combined with the above three methods as the corresponding detectors. The false-alarm rate is given as $P_{fa} = 10^{-3}$, and 10^5 times of Monte-Carlo trials are done. Note that the hybrid integration results for all range cells provided by the KT+FrFT and the proposed method are transformed from the CFCR domain to the range and Doppler domain for fair detection performance comparison. Fig. 7 demonstrates the detection probabilities of the three detectors versus different SNR levels. The detection results show that the detection performance of the proposed method is superior to the other two methods, thanks to its better LFM signal concentration and the low sidelobes. We can also find that the KT+FrFT has a little better detection probability than the MTD+TMC. The main reasons are that the MTD+TMC does not consider the RCM inside the frame, while the KT+FrFT can remove the RCM inside the frame and among the different frames, and the simulation configures a little high radial velocity and long CPI, which makes the difference. But the two methods still have similar detection performance due to
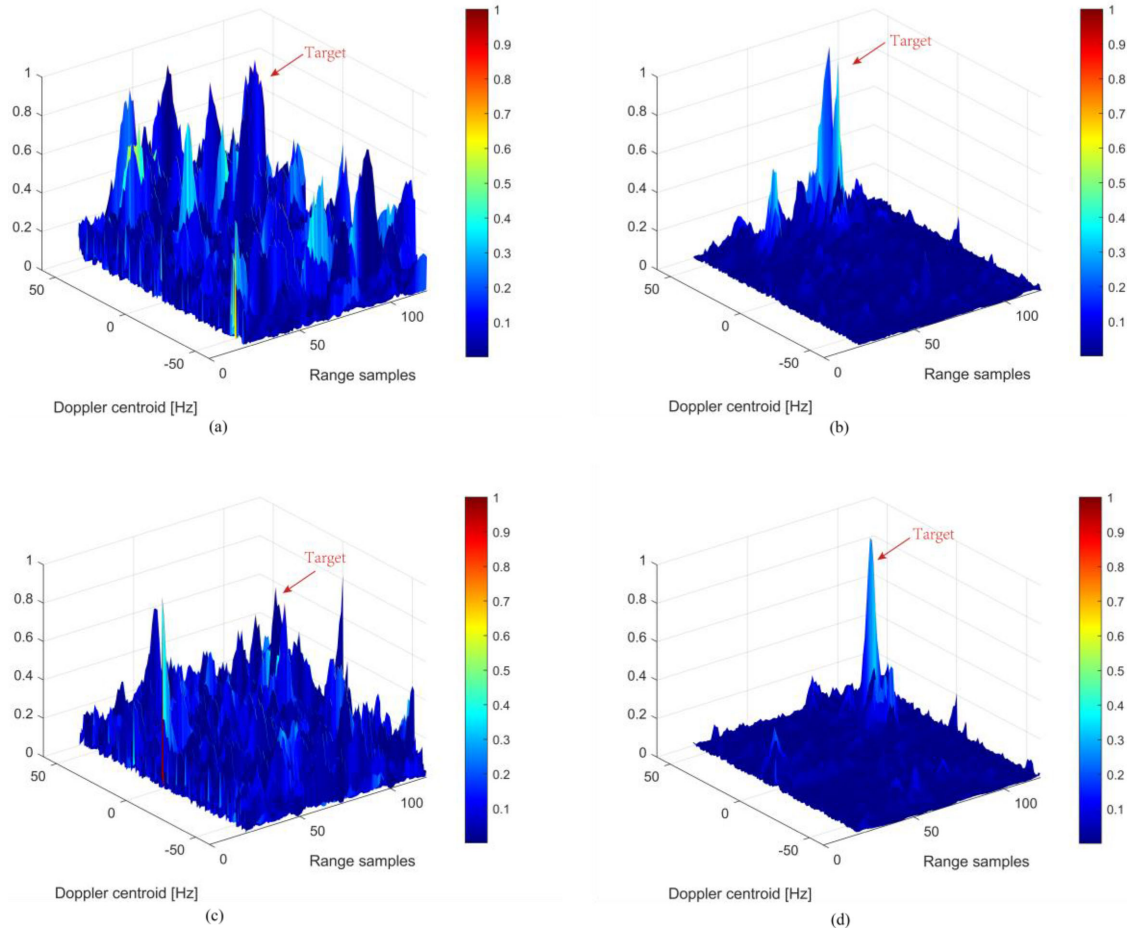
Fig. 10. Integration results for real experimental datasets via the MTD+TMC and the KT+LVD. (a) KUO LIN MTD+TMC result. (b) KUO LIN KT+LVD result. (c) WAN HAI 313 MTD+TMC result. (d) WAN HAI 313 KT+LVD result.

the rough range resolution. In other words, the KT+FrFT and the proposed method allow a longer CPI than the MTD+TMC.

B. Field Trial Results

To further demonstrate the effectiveness of the proposed method, field trials were carried out at Cyberport Waterfront Park in Hong Kong. A GPS satellite was selected as the non-cooperative illuminator of opportunity. Fig. 8(a) presents the receiver front-end. The receiver front-end has a pair of channels connecting to the circular antenna and the square antenna shown in Fig. 8(b). The circular antenna is a commercial off-the-shelf right-hand circular polarization antenna for the direct signal collection, while the square antenna is a custom left-hand circular polarization antenna with a 12 dB gain for the reflected signal collection. Two moving cargo ships shown in Fig. 9 were chosen as the objects of interest. Table III lists the voyage-related information of the ships provided by the automatic identification system as well as the information of the selected GPS satellite.

The MTD+TMC and the KT+FrFT have similar detection performance discussed in the previous section. For simplicity, only the MTD+TMC is employed for comparison here. Due to the close ranges and large sizes, both targets in Fig. 9 can be extracted from the background by the hybrid integration

TABLE III
EXPERIMENTAL PARAMETERS FOR FIELD TRIALS

KUO LIN	Length	170 m
	Average speed	7.5 m/s
	Vertical distance to the shore	804.9 m
WAN HAI 313	Length	213 m
	Average speed	7.2 m/s
	Vertical distance to the shore	938.6 m
GPS	Name	GPS BIIR-10
	pseudo random noise (PRN)	PRN22
	Elevation angle	25°~19°
	Azimuth angle	53°~46°

gains provided by the MTD+TMC and the proposed method. To present the difference between the two methods, coherent integration results are provided in Fig. 10. We can find that the peaks of the target signals by using the proposed method have good characteristics in terms of signal to background noise ratio in Fig. 10(b) and (d), whereas the peaks of the target signals by using the MTD+TMC cannot be easily distinguished from the disturbance in Fig. 10(a) and (c).

The range cross sections around the peak positions for the two cargo ships are demonstrated in Fig. 11(a) and (b). The blue dotted curves are generated by the MTD+TMC, while the red curves correspond to the proposed method. We can clearly see
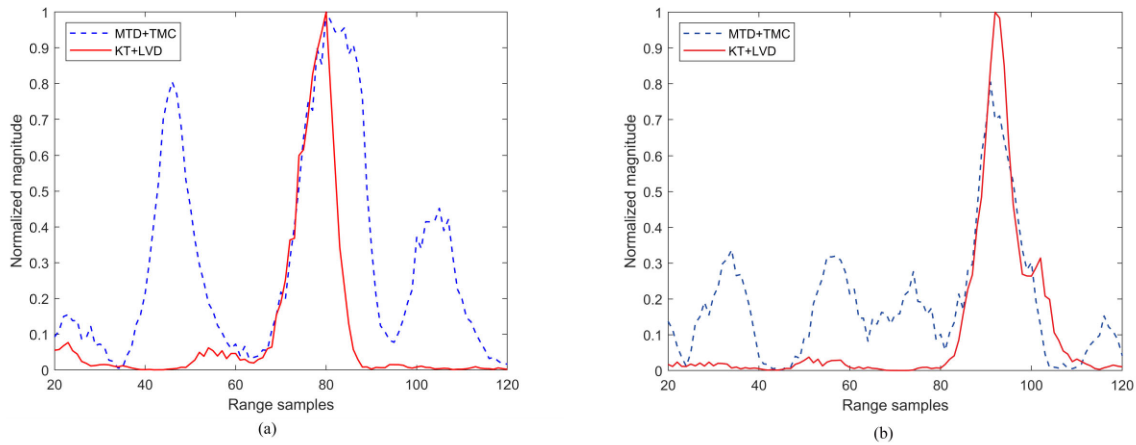
Fig. 11.   Range cross sections of the range Doppler maps in Fig. 10: (a) KUO LIN and (b) WAN HAI 313.

that both methods can provide sufficient integration gains for the target signal out of the background disturbance. However, the background fluctuations in the red curves are much lower than that in the blue dotted curves, which is conducive to improve the target detection performance. In addition, a higher integration gain is achieved by the proposed method in Fig. 11(b), as compared with the MTD+TMC.

In summary, the field trial results further show that the proposed method has a better target detection capability than the current known methods, thanks to the RCM correction by the KT and the excellent LFM signal concentration ratio provided by the LVD.

V. CONCLUSION

For the MTD, the low signal power on the ground level is the bottleneck of the GNSS-based passive radar. Increasing the observation time is an effective way to improve the target detection capability. However, the target motion involving the RCM and the DFM can lower the detection performance. To address the MTD issues, this article proposed a new hybrid coherent and noncoherent integration method known as the KT+LVD. First, we introduce the bistatic geometry and obtain a second-order polynomial expression of the bistatic range history. Then, the KT accomplishes the RCM compensation. The LVD performs the coherent integration operation for each frame and corrects DFM inside the frame. Before the noncoherent integration, Doppler frequency alignment operation is employed to eliminate DFM between multiple frames. Also, the computational complexity of the proposed method is analyzed. Finally, a simulation and field trials are carried out to validate the effectiveness of the proposed method and compare with other two target detection methods in [20], [24], and [25].

Both the simulated and the field trial results show that the proposed method achieves a better target detection capability than the other two methods. Furthermore, the analysis of the computational complexity indicates that the proposed method is in the same order as the other two methods. Therefore, the proposed method can be applied in the near real-time maritime MTD, thanks to the development of the modern parallel digital signal processing devices.

This article only considers the low speed targets, such as cargo ships, whose Doppler frequencies are lower than the pulse repetition frequency. However, for high-speed targets such as aircraft and guided missile, the Doppler ambiguity will occur. Our future work will take the Doppler ambiguity into account. Moreover, the use of multiple GNSS satellites can further improve the detection performance of the proposed method. So, how to extend the proposed method to the GNSS-based multistatic passive radar should be investigated in the future.

REFERENCES

[1] F. Colone, D. Langellotti, and P. Lombardo, "DVB-T signal ambiguity function control for passive radars," *IEEE Trans. Aerosp. Electron. Syst.*, vol. 50, no. 1, pp. 329–347, Jan. 2014.

[2] F. Colone, D. Pastina, and V. Marongiu, "VHF cross-range profiling of aerial targets via passive ISAR: Signal processing schemes and experimental results," *IEEE Trans. Aerosp. Electron. Syst.*, vol. 53, no. 1, pp. 218–235, Feb. 2017.

[3] R. Zemmari, M. Broetje, G. Battistello, and U. Nickel, "GSM passive coherent location system: Performance prediction and measurement evaluation," *IET Radar, Sonar Navig.*, vol. 8, no. 2, pp. 94–105, 2014.

[4] Q. Wang, C. Hou, and Y. Lu, "An experimental study of WiMAX-based passive radar," *IEEE Trans. Microw. Theory Techn.*, vol. 58, no. 12, pp. 3502–3510, Dec. 2010.

[5] M. Antoniou and M. Cherniakov, "GNSS-based bistatic SAR: A signal processing view," *EURASIP J. Adv. Signal Process.*, vol. 2013, no. 1, 2013, Art. no. 98.

[6] M. Antoniou, Z. Hong, Z. Zhangfan, R. Zuo, Q. Zhang, and M. Cherniakov, "Passive bistatic synthetic aperture radar imaging with Galileo transmitters and a moving receiver: Experimental demonstration," *IET Radar, Sonar Navig.*, vol. 7, no. 9, pp. 985–993, 2013.

[7] Z. Zeng, "Passive bistatic SAR with GNSS transmitter and a stationary receiver," Ph.D. dissertation, Dept. Electronic, Elect., Comput. Eng., Univ. Birmingham, Birmingham, U.K., 2013.

[8] F. Santi, M. Antoniou, and D. Pastina, "Point spread function analysis for GNSS-based multistatic SAR," *IEEE Geosci. Remote Sens. Lett.*, vol. 12, no. 2, pp. 304–308, Feb. 2015.

[9] T. Zeng, F. Liu, M. Antoniou, and M. Cherniakov, "GNSS-based BiSAR imaging using modified range migration algorithm," *Sci. China Inf. Sci.*, vol. 58, no. 8, pp. 1–13, 2015.

[10] M. Antoniou, M. Cherniakov, and H. Ma, "Space-surface bistatic synthetic aperture radar with navigation satellite transmissions: A review," *Sci. China Inf. Sci.*, vol. 58, no. 6, pp. 1–20, 2015.

[11] F. Liu, X. Fan, L. Zhang, T. Zhang, and Q. Liu, "GNSS-based SAR for urban area imaging: Topology optimization and experimental confirmation," *Int. J. Remote Sens.*, vol. 40, no. 12, pp. 4668–4682, 2019.

[12] F. Liu, M. Antoniou, Z. Zeng, and M. Cherniakov, "Coherent change detection using passive GNSS-based BSAR: Experimental proof of concept," *IEEE Trans. Geosci. Remote Sens.*, vol. 51, no. 8, pp. 4544–4555, Aug. 2013.

[13] Q. Zhang, M. Antoniou, W. Chang, and M. Cherniakov, "Spatial decorrelation in GNSS-based SAR coherent change detection," *IEEE Trans. Geosci. Remote Sens.*, vol. 53, no. 1, pp. 219–228, Jan. 2015.

[14] H. Ma *et al.*, "Maritime target detection using GNSS-based radar: Experimental proof of concept," in *Proc. IEEE Radar Conf.*, 2017, pp. 464–469.

[15] F. Pieralice *et al.*, "GNSS-based passive radar for maritime surveillance: Long integration time MTI technique," in *Proc. IEEE Radar Conf.*, 2017, pp. 508–513.

[16] X. He, T. Zeng, and M. Cherniakov, "Signal detectability in SS-BSAR with GNSS non-cooperative transmitter," *IEE Proc. Radar, Sonar Navig.*, vol. 152, no. 3, pp. 124–132, Jun. 2005.

[17] D. Pastina, M. Sedehi, and D. Cristallini, "Passive bistatic ISAR based on geostationary satellites for coastal surveillance," in *Proc. IEEE Radar Conf.*, 2010, pp. 865–870.

[18] J. Xu, J. Yu, Y.-N. Peng, and X.-G. Xia, "Radon-Fourier transform for radar target detection, I: Generalized Doppler filter bank," *IEEE Trans. Aerosp. Electron. Syst.*, vol. 47, no. 2, pp. 1186–1202, Apr. 2011.

[19] X. Chen, J. Guan, N. Liu, and Y. He, "Maneuvering target detection via Radon-fractional Fourier transform-based long-time coherent integration," *IEEE Trans. Signal Process.*, vol. 62, no. 4, pp. 939–953, Feb. 2014.

[20] Z. Li, F. Santi, D. Pastina, and P. Lombardo, "Multi-frame fractional Fourier transform technique for moving target detection with space-based passive radar," *IET Radar, Sonar Navig.*, vol. 11, no. 5, pp. 822–828, 2016.

[21] B. Carlson, E. Evans, and S. Wilson, "Search radar detection and track with the Hough transform. I. System concept," *IEEE Trans. Aerosp. Electron. Syst.*, vol. 30, no. 1, pp. 102–108, Jan. 1994.

[22] B. Carlson, E. Evans, and S. Wilson, "Search radar detection and track with the Hough transform. II. Detection statistics," *IEEE Trans. Aerosp. Electron. Syst.*, vol. 30, no. 1, pp. 109–115, Jan. 1994.

[23] V. Orlenko and Y. Shirman, "Non-coherent integration losses of wideband target detection," in *Proc. First Eur. Radar Conf.*, 2004, pp. 225–228.

[24] H. Ma *et al.*, "Maritime moving target indication using passive GNSS-based bistatic radar," *IEEE Trans. Aerosp. Electron. Syst.*, vol. 54, no. 1, pp. 115–130, Feb. 2018.

[25] D. Pastina *et al.*, "Maritime moving target long time integration for GNSS-based passive bistatic radar," *IEEE Trans. Aerosp. Electron. Syst.*, vol. 54, no. 6, pp. 3060–3083, Dec. 2018.

[26] X.-G. Xia, "Discrete chirp-Fourier transform and its application to chirp rate estimation," *IEEE Trans. Signal Process.*, vol. 48, no. 11, pp. 3122–3133, Nov. 2000.

[27] Y. Wei and G. Bi, "Efficient analysis of time-varying multicomponent signals with modified LPTFT," *EURASIP J. Adv. Signal Process.*, vol. 2005, no. 8, 2005, Art. no. 784762.

[28] X. Lv, G. Bi, C. Wan, and M. Xing, "Lv's distribution: Principle, implementation, properties, and performance," *IEEE Trans. Signal Process.*, vol. 59, no. 8, pp. 3576–3591, Aug. 2011.

[29] S. Luo, G. Bi, X. Lv, and F. Hu, "Performance analysis on Lv distribution and its applications," *Digit. Signal Process.*, vol. 23, no. 3, pp. 797–807, 2013.

[30] R. Perry, R. Dipietro, and R. Fante, "SAR imaging of moving targets," *IEEE Trans. Aerosp. Electron. Syst.*, vol. 35, no. 1, pp. 188–200, Jan. 1999.

[31] Y. Wang, J.-W. Li, J. Chen, H.-P. Xu, and B. Sun, "A parameter-adjusting polar format algorithm for extremely high squint SAR imaging," *IEEE Trans. Geosci. Remote Sens.*, vol. 52, no. 1, pp. 640–650, Jan. 2013.

[32] G. Bi and Y. Chen, "Fast generalized DFT and DHT algorithms," *Signal Process.*, vol. 65, no. 3, pp. 383–390, 1998.

[33] E. Sejdić, I. Djurović, and L. Stanković, "Fractional Fourier transform as a signal processing tool: An overview of recent developments," *Signal Process.*, vol. 91, no. 6, pp. 1351–1369, 2011.
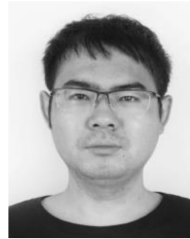
Zhenyu He received the B.S. and M.S. degrees from the School of Computer and Information, Hohai University, Nanjing, China, in 2012 and 2015, respectively. He is currently working toward the Ph.D. degree with the Department of Land Surveying and Geo-informatics, The Hong Kong Polytechnic University, Hong Kong.

His research interests include GNSS-based passive radar for moving target detection and GNSS-SAR imaging.
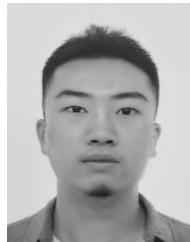
Yang Yang received the B.S. degree from PLA Information Engineering University, and the M.S. and Ph.D. degrees from the Hong Kong Polytechnic University, Hong Kong.

He is a Research Assistant with the Department of Land Surveying and Geo-informatics, The Hong Kong Polytechnic University. His research interests include GNSS software receiver and deformation detection based on GNSS-R technology.

Wu Chen is a Professor with the Department of Land Surveying and Geo-Informatics of the Hong Kong Polytechnic University. He has been actively working on GNSS related research for more than 30 years. His main research interests are geodesy and geodynamics, seamless positioning technologies, GNSS positioning and applications, system integration, GNSS performance evaluation, regional GPS network, and SLA.